Development of *X*-band single-cell dielectric disk accelerating structures

B. Freemire,[1,*] J. Shao,[2] S. Weatherly,[3] M. Peng,[2] E. Wisniewski,[2,3] S. Doran,[2] W. Liu,[2] C. Whiteford,[2] X. Lu,[2,4] S. Poddar,[1] E. Gomez,[1] J. Power,[2] and C. Jing[1,2,†]

[1]*Euclid Beamlabs, Bolingbrook, Illinois 60440, USA*
[2]*Argonne National Laboratory, Lemont, Illinois 60439, USA*
[3]*Illinois Institute of Technology, Chicago, Illinois 60616, USA*
[4]*Northern Illinois University, DeKalb, Illinois 60115, USA*

(Received 7 September 2022; accepted 12 June 2023; published 6 July 2023)

Short-pulse two-beam acceleration (TBA) is a promising advanced accelerator concept that may meet the luminosity and cost requirements of future large-scale linear colliders. Accelerating structures with high group velocity (on the order of 0.1c) are required in this scheme to reduce the filling time so as to efficiently accelerate the main beam with multiple bunches. In conventional accelerating structures such as metallic disk-loaded and dielectric-loaded, high group velocity usually implies low shunt impedance, which limits the rf-to-main-beam efficiency and causes a bottleneck in the overall wall-plug-to-main-beam efficiency. A dielectric disk accelerator (DDA) is a hybrid structure, which has geometry similar to metallic disk-loaded accelerators, but replaces the metal disks with dielectric disks to form the cells. Such a configuration could achieve simultaneous high group velocity and high shunt impedance, making a DDA a very attractive candidate for the short-pulse TBA approach by significantly improving power efficiency. In this manuscript, we present the start-to-end development of two *X*-band single-cell DDA prototypes, including the rf and mechanical design, fabrication, cold test, high power beam test, and post-test inspection. Of the two, a clamped structure performed better, achieving 102 MV/m accelerating gradient from 320-MW input power.

DOI: 10.1103/PhysRevAccelBeams.26.071301

I. INTRODUCTION

There are two major considerations involved in the realization of the next generation of high energy particle accelerators: the technology required to achieve the necessary beam energy and intensity and the cost to build and operate the accelerator. There has been significant effort devoted over the past few decades to addressing both of these issues [1]. Several accelerator schemes have been identified that offer the potential to deliver the required beam energy and intensity while reducing construction and operation costs. These generally fall into two categories: laser driven (laser wakefield [2,3] and dielectric laser [4,5]) and beam driven (plasma wakefield [6,7] and structure wakefield [8,9]) acceleration.

Two-beam acceleration (TBA) is an approach within the category of structure wakefield acceleration that is favorable in linear colliders [10–12]. In this approach, a high-charge drive beam traveling through a structure excites wakefields which are then used to accelerate a low-charge main beam in a parallel structure. The Argonne Wakefield Accelerator facility (AWA) [13] is currently focusing on the R&D of accelerator and beam physics for TBA, especially short-pulse TBA in which ~20 ns rf pulses are used. The pulse length, significantly shorter than that used in conventional structure-based acceleration, is chosen with the expectation of achieving an accelerating gradient (defined as $\frac{1}{L}\int_0^L E_z(z,t)dz$, where L is the length of the rf cell) over 270 MV/m based on evidence that the rf breakdown rate decreases with decreasing pulse length [14]. Recently, an *X*-band single-cell metallic disk-loaded structure was tested up to a gradient above 250 MV/m [15]. Such a gradient is significantly higher than state-of-the-art room-temperature normal-conducting *X*-band structures [16]. Achieving such a large accelerating gradient would reduce the footprint and construction cost of future colliders.

Short rf pulses, however, make it challenging to design accelerating structures that maintain reasonable rf-to-main-beam-efficiency. The group velocity needs to be very high (on the order of 0.1c) to fully fill the structure and leave enough flattop duration to accelerate the main beam while the shunt impedance also needs to be high to ensure strong beam-structure interaction to efficiently accelerate the main

*b.freemire@euclidtechlabs.com
†c.jing@euclidtechlabs.com

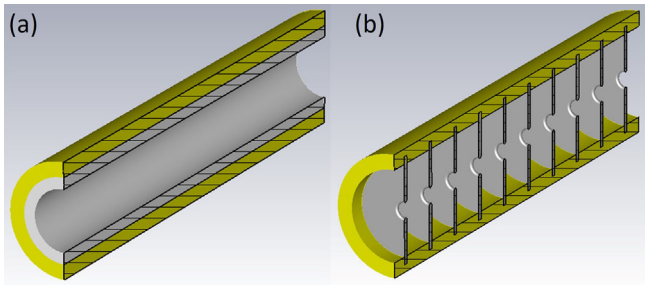

FIG. 1. Cutaway views of the geometries of a DLA (a) and DDA (b). The dielectric material is gray and the copper structure is yellow.

beam. The simultaneous high group velocity and high shunt impedance are usually contradictory in conventional structures, such as the prevailing metallic disk-loaded accelerator and the broadly studied dielectric-loaded accelerator [DLA, illustrated in Fig. 1(a)]. In addition, a high quality factor is also favorable to reduce the rf loss of the structure. In the proposed short-pulse TBA-based collider concept, the 3-TeV Argonne Flexible Linear Collider (AFLC), a 26-GHz DLA is chosen as the baseline design due to its high group velocity (0.11c), at the expense of relatively low shunt impedance ($r \sim 50$ ΩM/m) and quality factor (Q of 2300) [12,17]. The resultant rf-to-main-beam-efficiency is 27% and becomes the bottleneck of the overall wall-plug efficiency.

Recently, the concept of a dielectric-disk accelerator [Fig. 1(b)], originally proposed in the 1940s [18–20], has been revisited, based on the latest rf design and low loss dielectric materials. In a DDA, the cells are separated by dielectric disks, which naturally leads to large electromagnetic coupling and high group velocity for the TM_{01} mode. High dielectric constant materials are preferable to more traditional, lower dielectric constant materials (e.g., alumina) as they result in a larger accelerating gradient for similar geometries. Careful structure optimization as well as usage of an advanced dielectric material with high permittivity ($\epsilon_r \approx 50$) and low loss ($\tan\delta \approx 1 \times 10^{-4}$), allows a 26-GHz DDA to simultaneously achieve high group velocity (0.16 c), high shunt impedance ($r \sim 208$ ΩM/m), and high quality factor (Q of 6400) [21,22]. The corresponding rf-to-beam-efficiency reaches 39%, which is 50% higher than the baseline design. Compared to a DLA, the DDA also provides the additional advantage of easy tunability, the potential to be applied in constant-gradient structures, and relaxed fabrication constraints [21–23]. The disadvantages include field enhancement on the iris and complications arising at the triple junction (ceramic-metal-vacuum interface).

In this manuscript, we present the start-to-end development of two X-band 11.7-GHz single-cell traveling wave DDA prototypes, including the rf and mechanical design, fabrication, cold test, high power beam test, and post-test inspection. Each consisted of two dielectric disks forming the single dielectric cell and two copper irises on each end

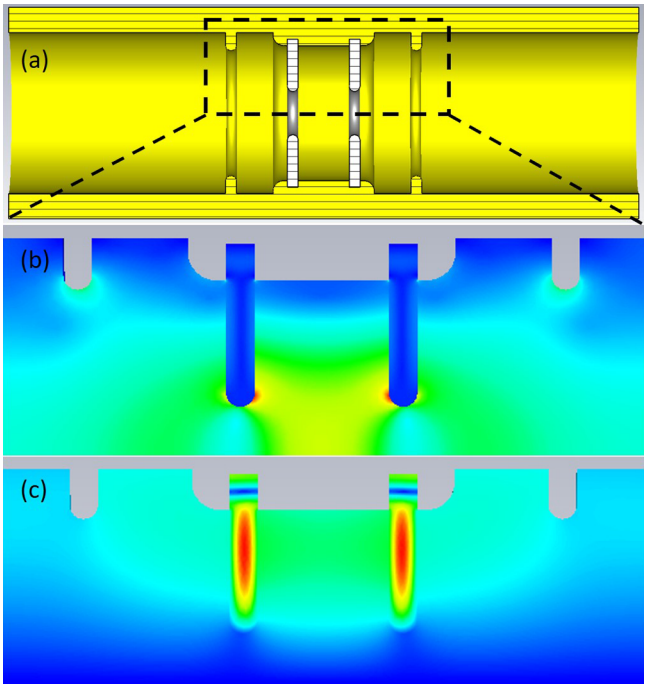

FIG. 2. Cross-sectional view of the brazed DDA prototype, showing the copper structure (yellow) and ceramic disks (white) (a). Contour field magnitudes from the area indicated by the dashed box in (a) projected on the centerline axis: electric (b) and magnetic (c); the dielectric and matching cells are shown.

forming cells for impedance matching [see Fig. 2(a)]. A brazed structure was designed and tested first, with the results guiding the design of a second, clamped structure. Practical considerations regarding the fabrication of each structure were considered, which particularly affected the area around the braze joint or triple junction (ceramic-metal-vacuum interface).

II. BRAZED STRUCTURE

The first DDA prototype designed, built, and tested was fabricated by brazing the ceramic disks to the copper body. This allowed the structure to be installed in the beamline and tested in air, though required significant effort to identify a successful brazing technique.

A. rf design

A barium titanate ceramic was used in the brazed DDA prototype. The dielectric properties of sample coupons were measured in a $TE_{01\delta}$ test cell resonator [24]. The measured values of ϵ_r and $\tan\delta$ were 50.1 ± 0.35 and $(8.00 \pm 0.32) \times 10^{-5}$, respectively, for which the error reported is the standard deviation of the measurement of ten coupons.

Both DDA prototypes were designed using CST Microwave Studio [25] and COMSOL [26]. Figure 2 shows

TABLE I. Simulated rf parameters of the brazed DDA prototype.

Parameter	Value	Unit
Dielectric constant	50.1	
Loss tangent	8.0×10^{-5}	
Quality factor	10,300	
Shunt impedance per unit length	176	MΩ/m
Group velocity/c	0.345	
Phase advance (multicell design)	$2\pi/3$	
$E_{\mathrm{surface,max}}/E_{\mathrm{acc}}$	1.84	

a cross-sectional view of the brazed DDA prototype and slices of the electric and magnetic fields. The structure was designed so that 100 MV/m accelerating gradient could be obtained when driven by a metallic power extractor providing 280 MW, ∼3 ns rise, ∼3 ns flattop, ∼3 ns decay (∼5 ns FWHM) rf pulses [9,27,28]. The rf parameters of the brazed DDA are listed in Table I. The DDA should be broadband, as to reduce the rise and fall time of the rf pulse. Excluding the couplers, the simulated value of S_{21} at 11.7 GHz was −0.026 dB, and the S_{11} 10-dB bandwidth was 1.28 GHz.

The two DDA structures utilized different couplers due to the brazed prototype being tested in air and the clamped prototype being tested in vacuum. The brazed prototype used TE to TM mode launch couplers with flanges that are reusable. These couplers were originally designed and built for testing of prior X-band structures and had a simulated bandwidth of 335 MHz [29].

Tuning was provided by push-pull studs brazed to the exterior of the structure. Each cell had four equally spaced tuners around the circumference. Each set of four tuners provided a ±3 MHz tuning range.

B. Mechanical design and fabrication

For both DDA structures, the most significant challenge in the mechanical design and fabrication was joining the ceramic disks to the copper body. Brazing ceramic to metal has historically been challenging [30–33]. There are a number of considerations involved, including the different coefficients of thermal expansion between ceramic and metal, the chemical reaction between the ceramic and whichever braze alloy is used, and the effect of the brazing conditions on the ceramic.

Braze trials were performed on coupons to determine the optimum procedure for the structure fabrication. The first braze attempt was done using an active braze alloy (ABA) at 835°C in a vacuum furnace. This was chosen because it is a standard alloy for brazing alumina (Al_2O_3) and reacts directly with the ceramic, negating the need for metallization. A thin copper sleeve was brazed to the circumference of a ceramic coupon. Figure 3 shows two test coupons prior to brazing and a portion of the braze joint. The mechanical

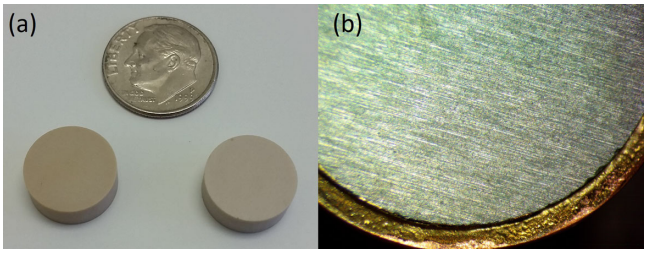

FIG. 3. Barium titanate test coupons (a). A portion of the ABA braze joint showing the darkened ceramic and copper sleeve (b).

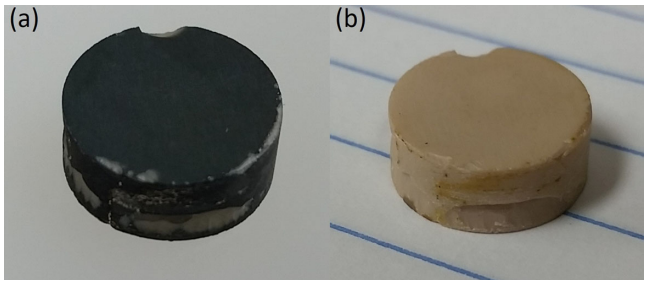

FIG. 4. The barium titanate coupon after the copper sleeve was removed postbraze (a). The coupon after the second recovery bake (b).

results of the brazing were adequate; however, there was a drastic darkening of the ceramic.

When the copper sleeve was removed, it was apparent that the layer of discolored ceramic was thin, as can be seen in Fig. 4(a). When the dielectric constant and loss tangent of the coupon were remeasured, the dielectric constant was ∼1% lower, while the loss tangent was ∼200 times larger. It is suspected that during the braze cycle, at elevated temperatures in a $\sim 1 \times 10^{-5}$ torr vacuum, oxygen debonded from the titanate and escaped the surface, resulting in the deterioration of the dielectric properties and darkening in color. An attempt was made to recover the dielectric properties by baking the coupon in an air furnace at ∼800 °C for 1 h. This resulted in drastic improvement of the loss tangent. A second recovery bake was performed, again at ∼800 °C for 1 h, which improved the loss tangent to within 26% of the original value. Table II lists the measured values of the dielectric constant and loss tangent before brazing, after brazing, and after the recovery bakes. A photo of the coupon after the

TABLE II. Dielectric properties of the barium titanate coupon before and after brazing, and after recovery baking cycles.

	Temperature (°C)	Time (min)	ϵ_r	tan δ
Prebrazing	⋯	⋯	50.2	8.15×10^{-5}
Postbrazing	835	⋯	49.7	1.43×10^{-2}
First bake	800	60	49.3	7.17×10^{-4}
Second bake	800	60	49.3	1.03×10^{-4}

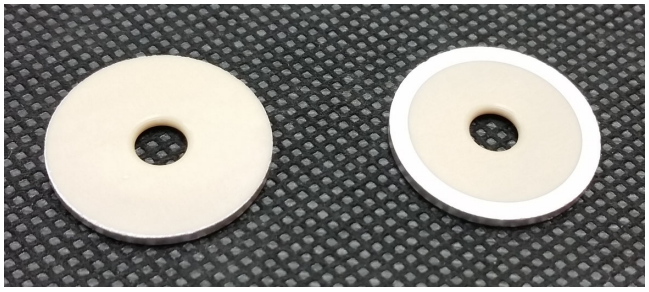

FIG. 5. Two of the machined barium titanate disks after metallization. The disk on the left was metallized on the circumference only, while the disk on the right was metallized on both faces to a certain radius in addition.

recovery bake is shown in Fig. 4(b). It can be seen that the color has almost returned to its prebrazed hue; hence the color of the ceramic is a good indication of the dielectric properties.

While the dielectric constant was not affected nearly as much as the loss tangent, it did decrease after brazing and baking, culminating at 1.8% lower than the original value. If a brazing method utilizing an ABA at a temperature above 800°C was pursued, the change in dielectric constant would have to be accounted for, in addition to a baking cycle in air after brazing to recover the loss tangent of the dielectric disks, followed by a cleaning cycle to remove the oxidation of the copper that would occur as a result.

An alternative brazing method was a low temperature braze using an alloy with a lower melting temperature. This method does not allow for an ABA, so the dielectric disks needed to be metallized prior to brazing. A silver-based paste was applied to the surface of the barium titanate disks, which were then fired at 850°C in air. Figure 5 shows two machined ceramic disks after metallization. No color change was observed for any of the 20 disks that were metallized, indicating that the elevated temperature did not adversely affect the dielectric properties.

The low temperature braze option was selected for fabrication of the DDA prototype because it did not require any postprocessing after the structure was brazed. Grooves were designed in the copper structure to locate the dielectric disks and provide alignment during brazing. The structure was machined in three pieces to allow for this. Two brazing cycles were performed. The first was a high temperature cycle to braze the stainless steel flanges and tuning pins to the copper body. Four push-pull pin tuners were brazed to the exterior of each cell (12 in total). The second was a low temperature cycle at 350°C using washers of a gold-tin alloy to braze the ceramic disks to the copper body. Table III lists relevant structure dimensions and Fig. 6 shows the mechanical design of the DDA prototype as well as a photo taken after brazing.

TABLE III. Brazed DDA prototype mechanical parameters.

Parameter	Value	Unit
Disk outer diameter	22.2	mm
Disk aperture diameter	5.2	mm
Matching cell aperture diameter	17.42	mm
Disk thickness	1.5	mm
Dielectric cell length	8.5	mm
Matching cell diameter	22.8	mm
Dielectric cell diameter	18.4	mm

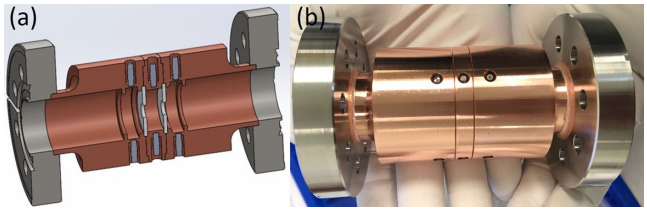

FIG. 6. A cutaway view of the brazed DDA prototype showing the ceramics disks and tuning pins (a). The prototype after brazing (b).

C. Cold test results

The brazed DDA structure was assembled with two mode launch couplers and connected to a network analyzer via WR90-to-SMA adapters. Figure 7 shows the comparison between the simulated (including the couplers) and measured S parameters. The measured (simulated) values of S_{11} and S_{21} at 11.7 GHz were −29.1 (−17.9) dB and −0.50 (−0.16) dB, respectively, and the S_{11} 10-dB bandwidth was ∼290 MHz, in reasonable agreement with the simulated coupler bandwidth of 335 MHz. The slightly larger simulated reflection is due to fabrication errors in the couplers, which, when measured together without the DDA, have an S_{11} value of −22.9 dB, compared to a simulated value of −29.0 dB. By changing the length of the circular waveguide section in the model including the

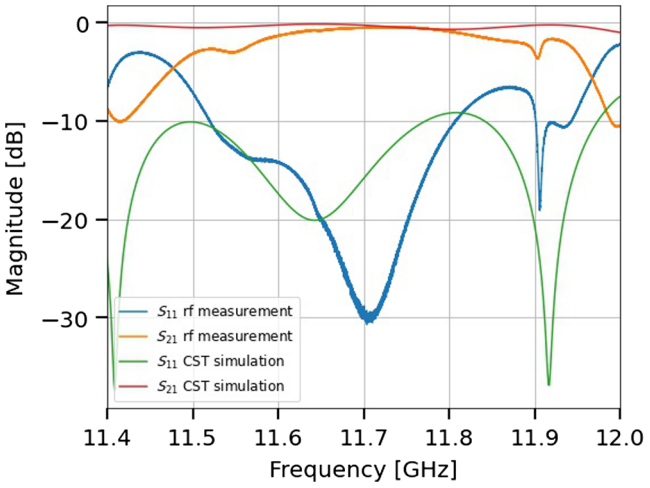

FIG. 7. Measured (blue and orange) and simulated (green and red) S-parameters for the brazed DDA prototype including couplers.

DDA, the simulated reflection at 11.7 GHz reached as low as −35.8 dB.

A bead-pull was not performed prior to high power testing for several reasons: the measured reflection was sufficiently small, this structure was used to accelerate a beam, and priority was given to maintaining cleanliness of the structure as it shared the same vacuum system as the drive beamline.

D. High power test results

High power testing was conducted at the AWA facility. The 65-MeV drive beamline was used to generate rf power with an *X*-band metallic power extraction and transfer structure (PETS) [9,27,28]. High-charge electron bunch trains are focused into the PETS by quadrupoles, exciting wakefields inside [29]. For the DDA experiments, the PETS was capable of generating ∼300 MW output rf power from an eight-bunch train of ∼400 nC total charge operated at a 2-Hz repetition rate [28]. The output rf pulse was ∼9 ns long, comprised of a ∼3 ns rising edge, ∼3 ns flattop, and 0–3 ns falling edge. The DDA prototypes were connected to the output port of the PETS via the WR90 waveguide. Two integrating current transformers (ICTs) [34] located before and after the PETS were used to measure the drive beam charge. During the brazed prototype high power test, rf pickup antennas were installed at the outputs of the PETS and DDA to measure the input and output power for the DDA [28]. During the clamped prototype high power test, bidirectional couplers were installed at the outputs of the PETS and DDA for the same purpose [28]. Cameras were installed at the ends of the DDA structures to look for light produced by multipacting or breakdown. Figure 8 shows a schematic of the experimental setup for the clamped prototype high power test.

The rf signals were recorded on a Tektronix DSA 72504D oscilloscope with a 50 GS/s sampling rate and a 20-GHz bandwidth. The ICT signals were recorded on a slower oscilloscope due to their low frequency primary component. Breakdown events were identified by the characteristic fast discharge of the rf amplitude, as well as light detection using the cameras. Multipactor activity was identified by decreased rf amplitude during the rf pulse and light detection using the cameras.

The brazed DDA prototype was conditioned by gradually increasing the charge and number of bunches sent through the PETS, which resulted in a larger power delivered to the DDA. At low input power, no light emission from the DDA was detected by the cameras and the transmitted rf pulse amplitude and shape agree well with the simulation—Fig. 9—suggesting no loading or breakdown occurred inside the structure.

When the DDA input power was higher than 10 MW, the transmitted rf power was lower than expected based on the transmission loss through the DDA (not including the waveguide losses, which were not measured for this experiment) and the discrepancy became larger as the input power increased, as illustrated in Fig. 10, indicating significant multipacting was occurring. The additional loss of the waveguide, which was measured during the clamped prototype experiment, was not enough to account for the measured transmitted power.

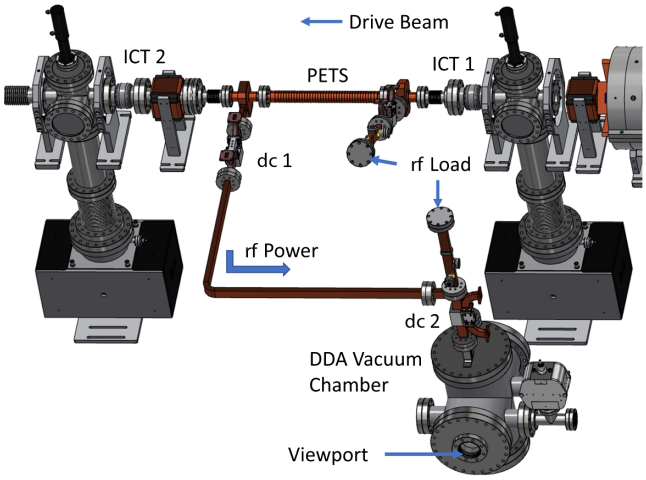

FIG. 8. Layout of the experimental beamline at the AWA, showing the PETS, clamped DDA prototype vacuum chamber, and locations of the bidirectional couplers, viewport, and ICTs.

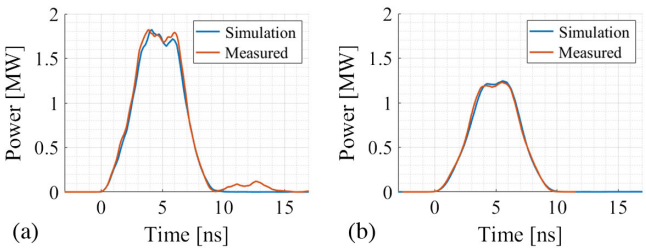

FIG. 9. The input (a) and output (b) rf waveforms for the brazed DDA prototype during single-bunch operation at 1.75-MW input power. The measured data (red) agree well with the simulated values (blue).

Figure 11 shows representative camera snapshots of the faces of the upstream and downstream ceramic disks during eight-bunch high power operation. The light was visible above ∼40 MW input power, only around the circumference of the ceramic disks—no light was observed coming from the irises. Light emission indicates localized plasma formation, which could be caused by strong field emission current or rf breakdown. When light was observed, the input power was kept constant in an effort to condition the structure. Over time, a large portion of the emitters stopped emitting, however, no amount of conditioning could completely remove them.

Figure 12 shows the transmitted rf power at the beginning and end of conditioning at ∼38 MW input power

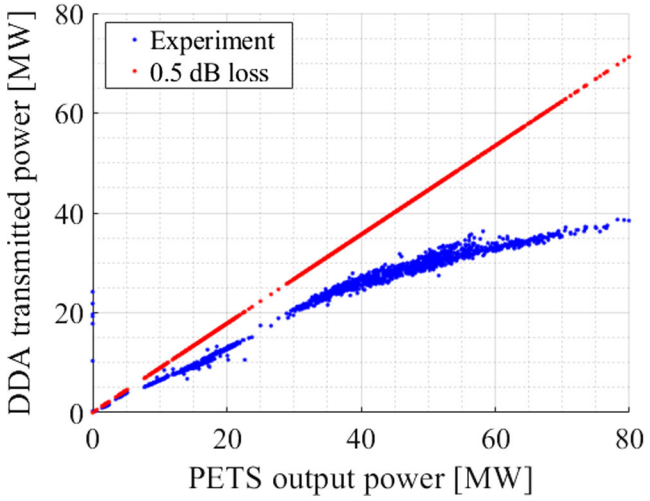

FIG. 10. Transmitted power through the brazed DDA prototype vs the input power as measured during eight-bunch operation. The blue dots represent the experimental results. The red dots represent the expectation with 0.5-dB loss, based on the measured transmission of the DDA structure.

during an eight-bunch operation. Significant loading at the beginning of operation was observed, with no appreciable flattop rf waveform. With time, some transmitted power was recovered, however, the expected transmission was never achieved. The source of this loading is believed to be the emitters around the circumference of the dielectric disks

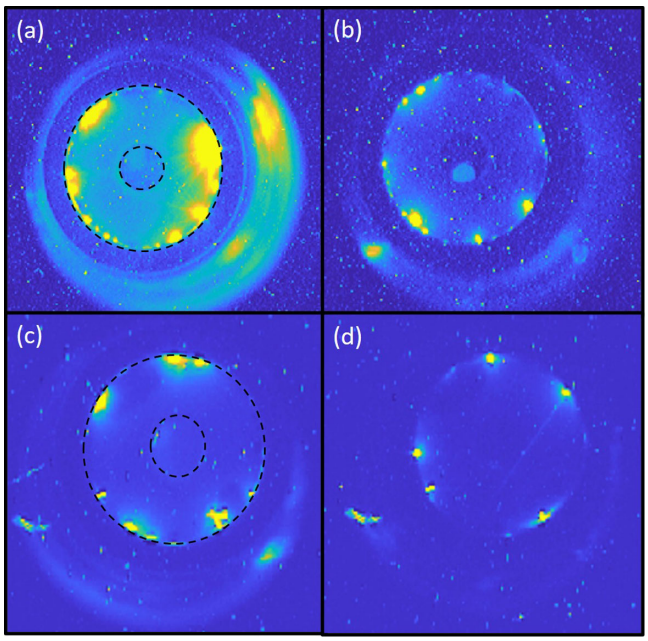

FIG. 11. Snapshots of the face of the upstream (top) and downstream (bottom) ceramic disks during conditioning for eight-bunch operation at ~65 MW. The earliest time is on the left and the latest on the right. The inner and outer diameters of the dielectric disks have been outlined for both disks in (a) and (c).

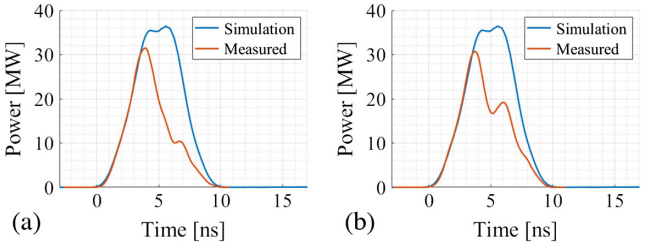

FIG. 12. Representative rf waveforms recorded before (a) and after (b) the conditioning process for eight-bunch operation at ~38 MW input power (red—measured data, blue—simulated).

from which light was visible, as illustrated in Fig. 11. The improved rf transmission with time, coupled with the decrease in the number of light emission sites, indicates that conditioning of the metal in and around the braze joint occurred during high power operation.

There is no sufficient evidence to attribute the less-than-expected power transmission entirely to multipacting or breakdown. While it is questionable whether the short rf pulse length (~10 ns) allows for the resonant condition needed for multipacting to exist, the multipactor effect has been observed in *X*-band dielectric-loaded structures with 150-ns pulses [35] and simulations indicate that multipactor can develop over 1's to 10's of nanoseconds timescales (10's to 100's of rf periods in the case of the DDA reported here) [36–41]. Conversely, none of the typical signs of breakdown were present (full rf reflection with a short rise time or intense flashes of light), although this may be a result of operating in the so-called breakdown insensitive regime due to the short rf pulse length [15,42].

It is well known that the ceramic in dielectric-loaded accelerating structures does not condition, but rather after reaching the surface electric field corresponding to the dielectric strength of the material, breaks down, after which the gradient is limited to that value [43–45]. The fact that the transmitted rf power could be improved through conditioning indicates the source of loading in the brazed DDA prototype stemmed from the triple junction as opposed to the ceramic disks.

At ~80 MW input power, a significant multipactor or breakdown was observed in the rf waveform of the brazed DDA prototype, which could not be conditioned away. The operation ceased with a maximum input power of 79.9 MW, corresponding to a peak electric field of 85.8 MV/m on the surface of the ceramic disks, or 46.6 MV/m accelerating gradient.

E. Postrun results

A thorough inspection was performed with the goal of determining the reason for the field emission observed near the triple junction. The structure was cut parallel to both faces of each ceramic disk using a wire EDM to not damage the surface. One of the two disks was cleaned and measured with a scanning electron microscope (SEM) and then run

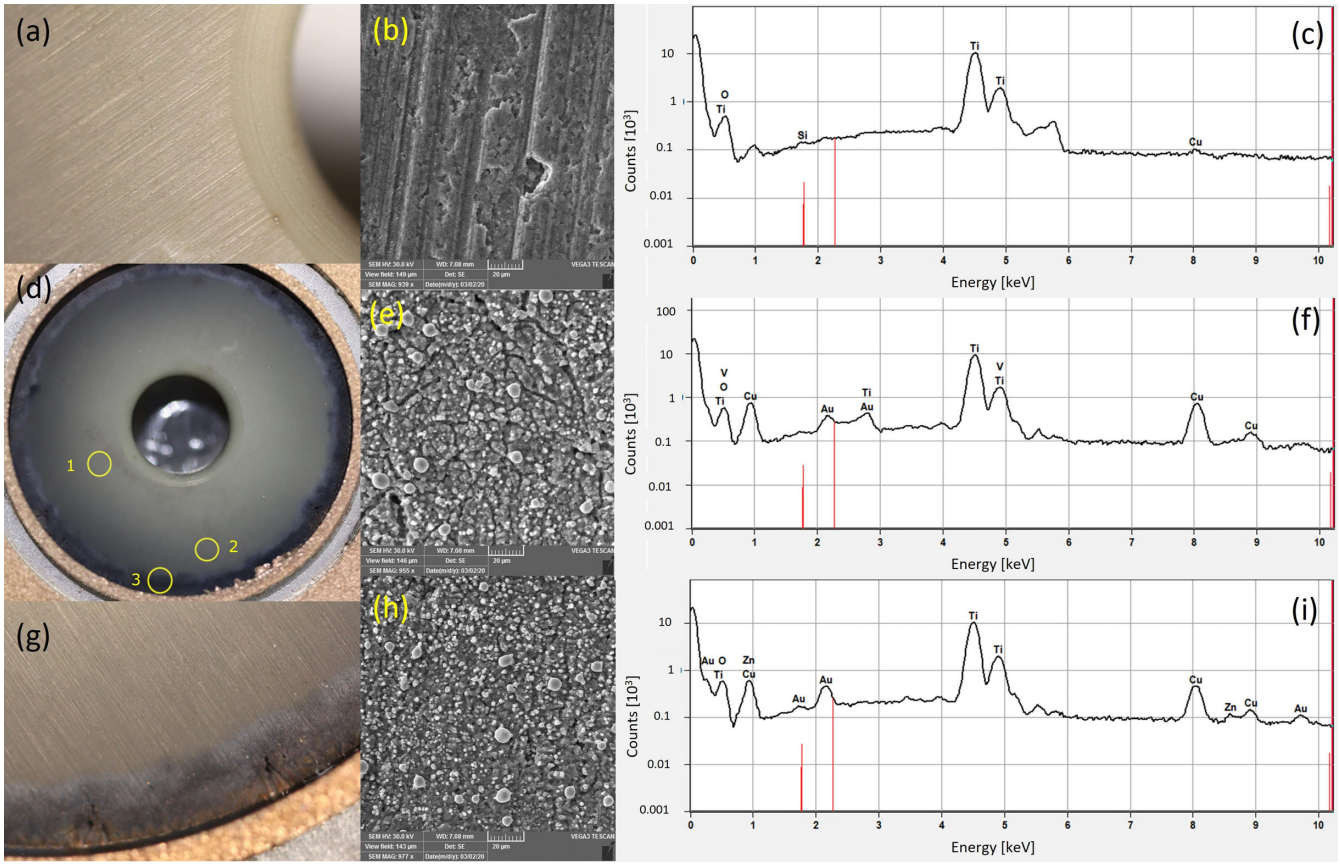

FIG. 13. SEM and EDX results from the interior face of one barium titanate disk that was tested at high power. The entire face is shown in (d), with the locations of SEM and EDX data collected shown: 1—(b) & (c), 2—(e) & (f), 3—(h) & (i). Closer images of the iris (a) and braze joint (g) are shown as well.

through energy-dispersive x-ray spectroscopy (EDX) at the Center for Nanoscale Materials at Argonne National Laboratory. The photos on the left of Fig. 13 show the interior face of the upstream disk. SEM and EDX measurements were taken at the three locations labeled. The surface of location 1 (near the iris) shows the same topography as a disk that was not tested at high power. The surfaces of the locations 2 and 3 (near the braze joint and midway between the iris and braze joint) have a much more granular topography, resulting from the ceramic having been damaged.

The EDX results reveal the presence of the gold brazing alloy as well as copper, indicating that these metals were deposited on the surface of the ceramic disks as a result of breakdown near the braze joint. Similar results were obtained on the exterior faces of the disks, indicating there is no asymmetry in the electron activity at the triple junction.

As shown in Fig. 2, the location of the maximum electric field on any surface of the structure was the interior portion of the disk iris, which would be the most likely place for breakdown to occur. Instead, the ceramic disks had significant damage over the entire circumference at the braze joint, with several pits visible in the darkened areas. The iris was free from damage but did contain a number of deposits of metal from the breakdown in the triple junction region—see Fig. 14.

Prior to the visual inspection, the *S*-parameters were remeasured and a bead pull was performed. The results of the *S*-parameter measurement are shown in Fig. 15. The transmission decreased and reflection increased, indicative of the damage shown in Fig. 13. The results of the bead-pull are shown in Fig. 16. Both simulated and measured data

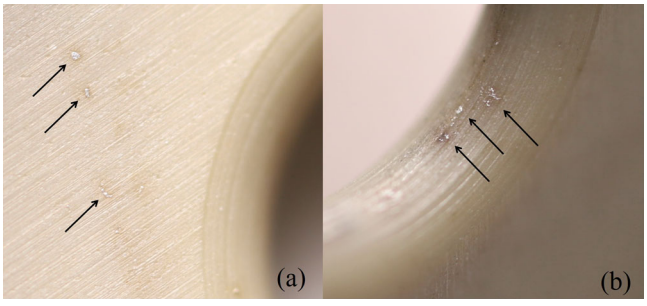

FIG. 14. The irises of both upstream (shown here) and downstream disks contained deposits of metal—most likely a result of breakdown at the braze joint.

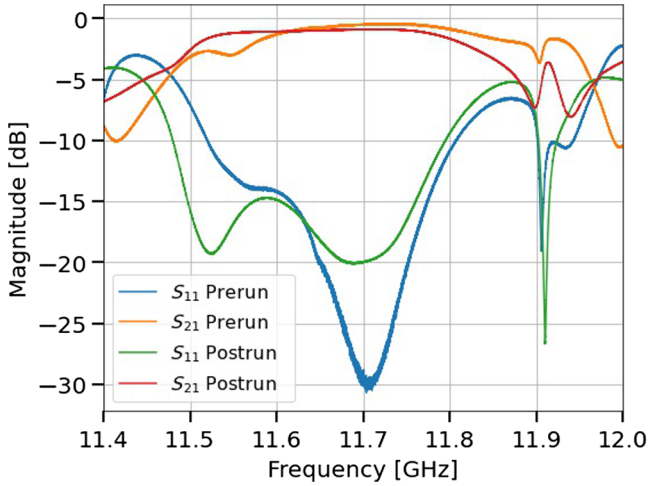

FIG. 15. Measured *S*-parameters before (blue and orange) and after (green and red) the high power test for the brazed DDA prototype.

have been normalized to their respective maximum values. The ratios of the peak field within the dielectric cell and matching cells are consistent between the postrun data and simulation, though the ratio between the peak field and that in the waveguide sections disagrees. Additionally, more oscillations of the field in the waveguide were measured than predicted in simulation. The bead-pull measurement of the clamped DDA prototype done after the high power test (Fig. 24), which did not have significant damage, shows good agreement with the simulation for the electric field in the cells, and waveguide sections. The discrepancy between the bead-pull measurement and simulation can therefore be attributed to a combination of machining errors in the waveguide section and damage that occurred during the high power test.

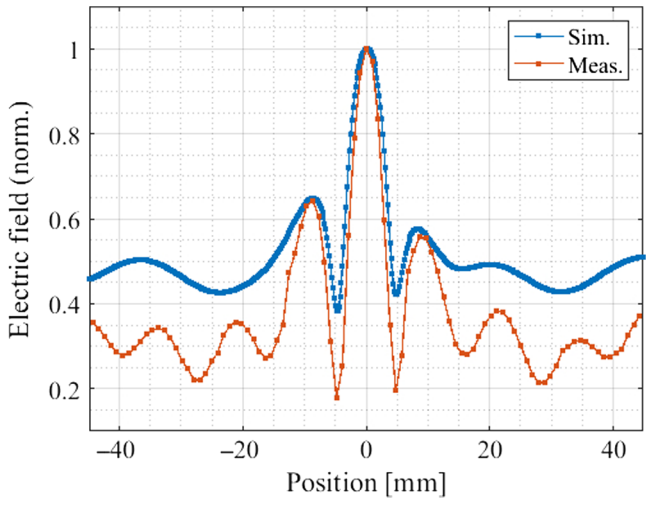

FIG. 16. Electric field on axis at 11.7 GHz normalized to the maximum electric field for the brazed DDA prototype. Measured values after the high-power run—orange; simulated values—blue.

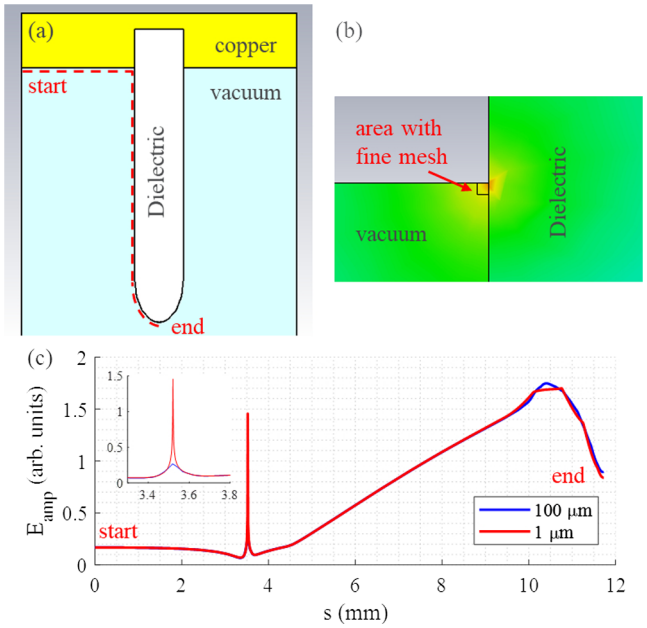

FIG. 17. The electric field amplitude plotted in (c) follows the dashed path shown in (a). The mesh density in the triple junction region was increased (b). The inset in (c) shows the difference in the field at the triple junction between coarse and fine mesh.

Due to the damage on the ceramic disks being almost exclusively contained to the area around the braze joint, the electromagnetic field distribution in that area was reexamined in the simulation model. As shown in Fig. 17, increasing the local mesh density revealed the magnitude of the electric field at the braze joint approached that on the iris of the ceramic disk, where the field is maximal. The field enhancement at the triple junction is similar for the interior and exterior sides of the disk, consistent with the damage observed on both sides posthigh power run. This field enhancement at the braze joint therefore led to strong field emission and, at higher gradients, breakdown in this region, which resulted in damage to the surface of the ceramic; limiting the achievable electric field in the DDA prototype.

Light emission from the triple junction during high power operation, improved rf power transmission through conditioning, visual inspection of the disks after the high power test, and SEM and EDX results all indicate that the braze joint in the brazed DDA prototype was the limiting factor for the accelerating gradient. This indicates there is no fundamental problem with brazed dielectric disk accelerators, rather the engineering of the braze joint needs to be improved.

III. CLAMPED STRUCTURE

A. rf design

The clamped DDA prototype utilized a calcium-titanium-lanthanum-aluminum-oxide ceramic due to the unavailability of the barium titanate ceramic during the

design and fabrication phases. The dielectric properties of three sample coupons of different sizes were measured in a $TE_{01\delta}$ test cell resonator at frequencies ranging from 3.8 to 7.4 GHz. The measured values of ϵ_r and $\tan\delta$ were then extrapolated to 11.7 GHz, resulting in 47.7 and 3.44×10^{-4}, respectively.

Figure 18 shows a cross-sectional view of the electric and magnetic fields of the clamped DDA prototype and Table IV lists the rf properties. The structure was designed so that 100 MV/m accelerating gradient could be obtained from a PETS output of 308 MW.

To avoid enhancement of the electric field at the triple junction, the interface was designed as shown in Fig. 19, with elliptic rounding added to the ceramic and copper. The electric field on the copper edge ($s = 3.5$ mm in Fig. 19d) is less than half that on the ceramic iris, while the field at the triple junction is significantly less. A mesh density convergence study was performed [Figs. 19(c) and 19(d)], confirming the low electric field on the copper edge and at the triple junction.

The clamped prototype used TE to TM mode converters that were brazed to the matching cell sections. Excluding the couplers, the simulated value of S_{21} at 11.7 GHz was −0.022 dB, and the S_{11} 10-dB bandwidth was > 1.25 GHz. The simulated bandwidth of the TE to TM mode converter couplers was ≈750 MHz. This is sufficient to fill structure within the rf pulse length.

Tuning was provided by push-pull studs brazed to the exterior of the structure. Each cell had four equally spaced tuners around the circumference. As with the brazed prototype, each set of four tuners provided a ±3 MHz tuning range.

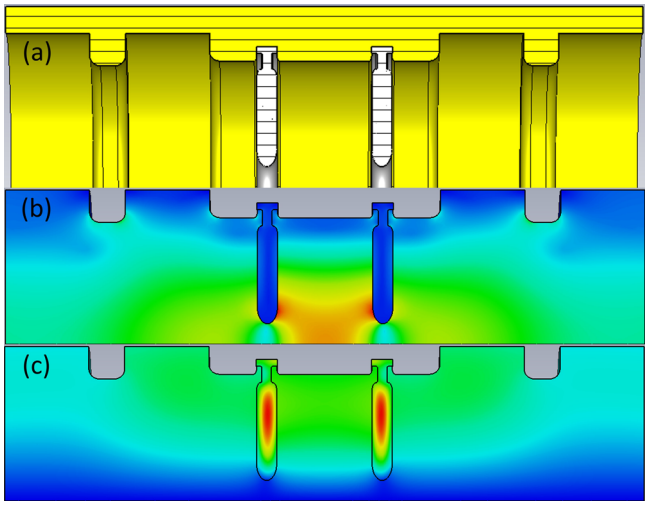

FIG. 18. Cross sectional view of half of the clamped DDA prototype, showing the copper structure (yellow) and ceramic disks (white) (a). Contour field magnitudes projected on the centerline axis: electric (b) and magnetic (c); the dielectric and matching cells are shown.

TABLE IV. Simulated rf parameters of the clamped DDA prototype.

Parameter	Value	Unit
Dielectric constant	47.7	
Loss tangent	3.44×10^{-4}	
Quality factor	8500	
Shunt impedance per unit length	174	MΩ/m
Group velocity/c	0.270	
Phase advance (multicell design)	$2\pi/3$	
$E_{\text{surface,max}}/E_{\text{acc}}$	1.44	

B. Mechanical design and fabrication

Ensuring good, consistent contact between the ceramic disks and copper parts while minimizing field enhancement was the focus of the clamped prototype design. To properly locate the ceramic disks within the structure without brazing them in place, each was clamped between two copper sections. As a result, the copper structure was fabricated in three pieces, with grooves in the central copper piece to place the ceramic disks. Because the clamping mechanism did not provide a vacuum seal, the entire clamped DDA prototype was tested in a vacuum chamber. Mode converters were designed and built, then

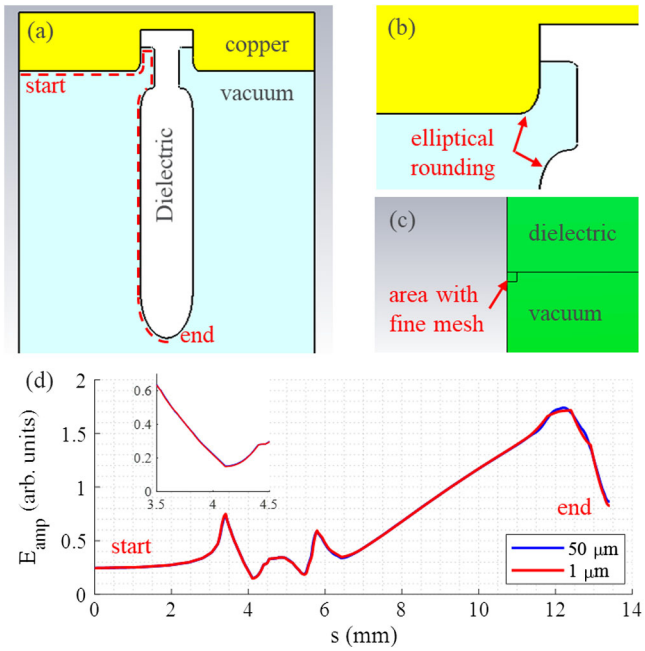

FIG. 19. The ceramic-metal interface for the clamped DDA prototype, with the path of the plotted field shown (a). Closer detail highlighting elliptical rounding (b). Simulation domain with increased mesh density, corresponding to the location of the triple junction (c). Electric field amplitude plotted along the curve in (a) showing decreased field in the region of the triple junction (d), independent of mesh density. The inset in (d) shows the field at the triple junction.

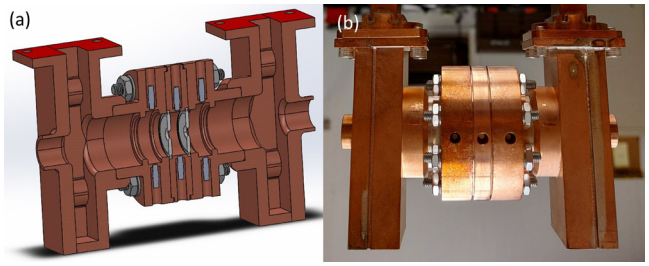

FIG. 20. A cutaway view of the clamped DDA prototype showing the ceramic disks, tuning pins, and couplers (a). The structure after assembly (b).

brazed to the ends of the DDA structure. Four push-pull pin tuners were brazed to the exterior of each cell, at a location where the copper wall was thin. The two copper end pieces and central body were held together with eight sets of threaded rods, nuts, and washers. Elliptic rounding was added to the copper edges nearest the ceramic to minimize field enhancement. A groove in the ceramic was added in the area of the rounded copper edges to further reduce the electric field. The irises of the ceramic disks were also rounded elliptically to decrease the maximum electric field on the surface of the ceramic. Figure 20 shows a cutaway view of the mechanical design including couplers and a photo of the assembled structure. Table V lists relevant structure dimensions.

C. Cold test results

Prior to the high power test, the clamped DDA prototype was assembled and the S-parameters were measured. An Agilent N5230C vector network analyzer and WR90 to SMA adapters were used. Figure 21 shows the measured and simulated (including couplers) S-parameters. The measured (simulated) values of S_{11} and S_{21} at 11.7 GHz were -17.8 (-39.5) dB and -0.652 (-0.0079) dB, respectively, and the S_{11} 10-dB bandwidth was $> 640(450)$ MHz. The small differences can be attributed to structural dimension differences in the DDA prototype or dielectric constant variation.

As with the brazed prototype, a bead pull was not performed on the clamped prototype prior to high power testing.

TABLE V. Clamped DDA prototype mechanical parameters.

Parameter	Value	Unit
Disk outer diameter	20.9	mm
Disk aperture diameter	3.0	mm
Matching cell aperture diameter	18.0	mm
Disk thickness	1.5	mm
Dielectric cell length	8.54	mm
Matching cell diameter	22.8	mm
Dielectric cell diameter	18.7	mm

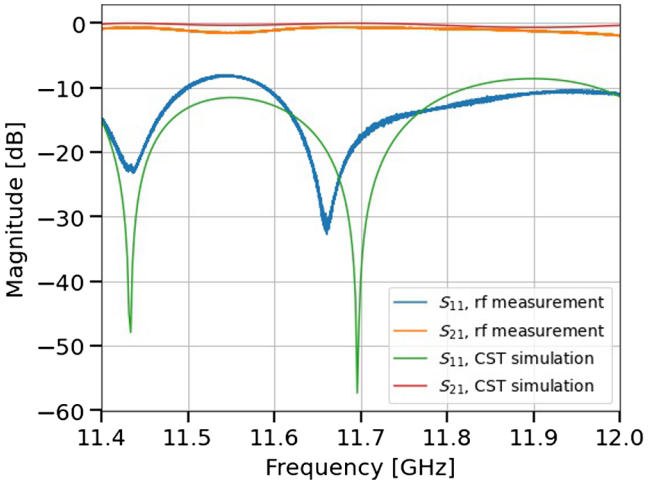

FIG. 21. Measured (blue and orange) and simulated (green and red) S-parameters for the clamped DDA prototype including couplers.

D. High power test results

The clamped DDA prototype was conditioned to high power gradually by slowly increasing the total beam charge of an eight-bunch electron train sent through the PETS, corresponding to a gradual increase in the input power to the DDA. Figure 22 shows representative plots of the input and output power for the cases of low and high charge through the PETS. For both, the output power agrees well with the input power and measured transmission loss through the waveguide and DDA. Variations in the input rf power produced by inconsistent bunch charge can be seen. The peak rf power was found by taking the average over 0.3 ns around the maximum in the flattop region.

Figure 23 shows the measured output power from the DDA versus the input power. The measured power transmitted through the clamped DDA matches the expectation, taking into account losses in the waveguide and DDA structure, very well up to the maximum input power. This indicates that no significant multipacting took place during the high power test.

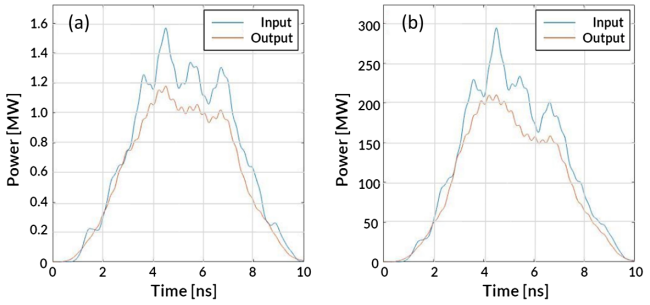

FIG. 22. Representative plots of the clamped DDA input (blue) and output (red) power at ∼1.5 MW (a) and ∼300 MW (b).

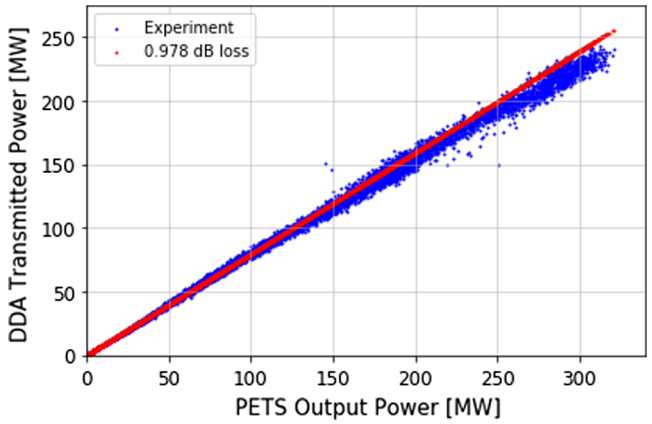

FIG. 23. Transmitted power through the clamped DDA prototype vs the input power. The blue dots represent the experimental results. The red dots represent the expectation accounting for the measured transmission loss in the DDA and waveguide.

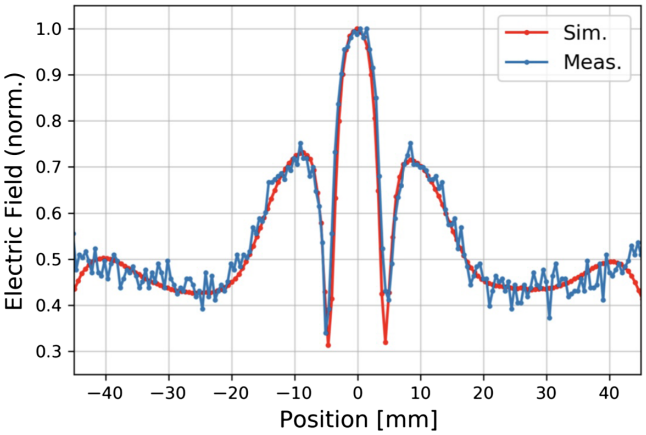

FIG. 24. Normalized electric field on axis at 11.7 GHz for the clamped DDA prototype. Measured values after the high-power run—blue; simulated values—red.

No evidence of breakdown was observed in the rf or light signals during the high power test. Around 200 MW input power, a faint light was observed coming from the downstream side of the structure, though it stopped after ≈15 min of conditioning; no other light was observed.

The clamped DDA prototype operated stably at the maximum output power from the PETS, 321 MW, corresponding to a peak electric field of 147 MV/m on the surface of the ceramic disks, or an accelerating gradient of 102 MV/m.

E. Postrun results

A bead-pull was performed on the clamped DDA prototype after the high power test; the results are shown in Fig. 24. The measured electric field on axis is in good agreement with the simulated values, indicating no damage to the structure occurred during high power testing.

The clamped DDA prototype was disassembled and inspected. No evidence of damage was present on the ceramic disk irises or faces. Figure 25 shows a photo of the iris of the downstream disk, as well as EDX results showing the elemental spectrum. Only elements comprising the ceramic were present, indicating no copper was deposited on the ceramics as a result of the breakdown.

Figure 26 shows photos taken of both faces of each ceramic disk as well as the two matching cells. No damage was present on the upstream ceramic disk and matching cell. There was one area of discoloration near the circumference of the ceramic on the interior face of the downstream disk. Photos of the exterior face of the downstream disk show discoloration and damage on approximately one quarter of the circumference of the disk and nearby copper region. Further damage is evident on the copper face of both the central and mating downstream piece, outside the rf field region. This suggests the clamping force was not uniform azimuthally, leading to rf field leaking into some regions between the two copper pieces, resulting in multipacting and/or arcing between the two. This was likely the source of the faint light emanating from the downstream side of the structure observed briefly during the high power test.

The lack of damage on any surface within the rf volume coupled with the good agreement between the expected and measured transmitted power indicates that with proper assembly design and procedure, a clamped DDA should be free from multipactor and breakdown at electric fields exceeding 150 MV/m on the surface of the ceramic.

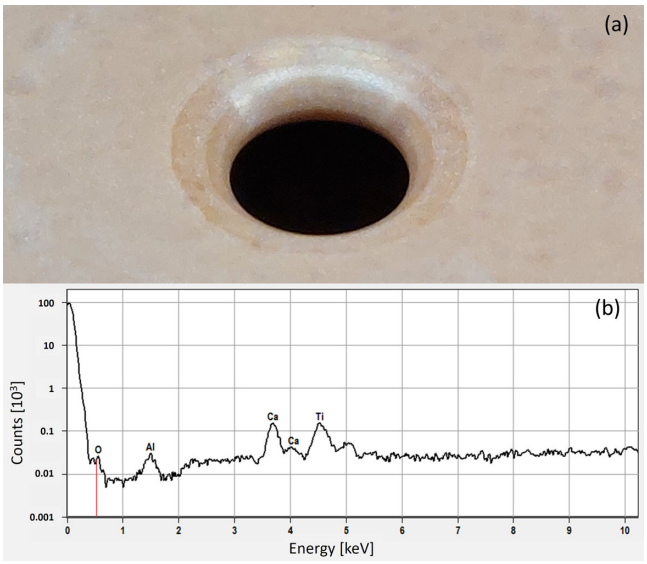

FIG. 25. Photo of the downstream ceramic disk iris posthigh power run (a). EDX results (b).

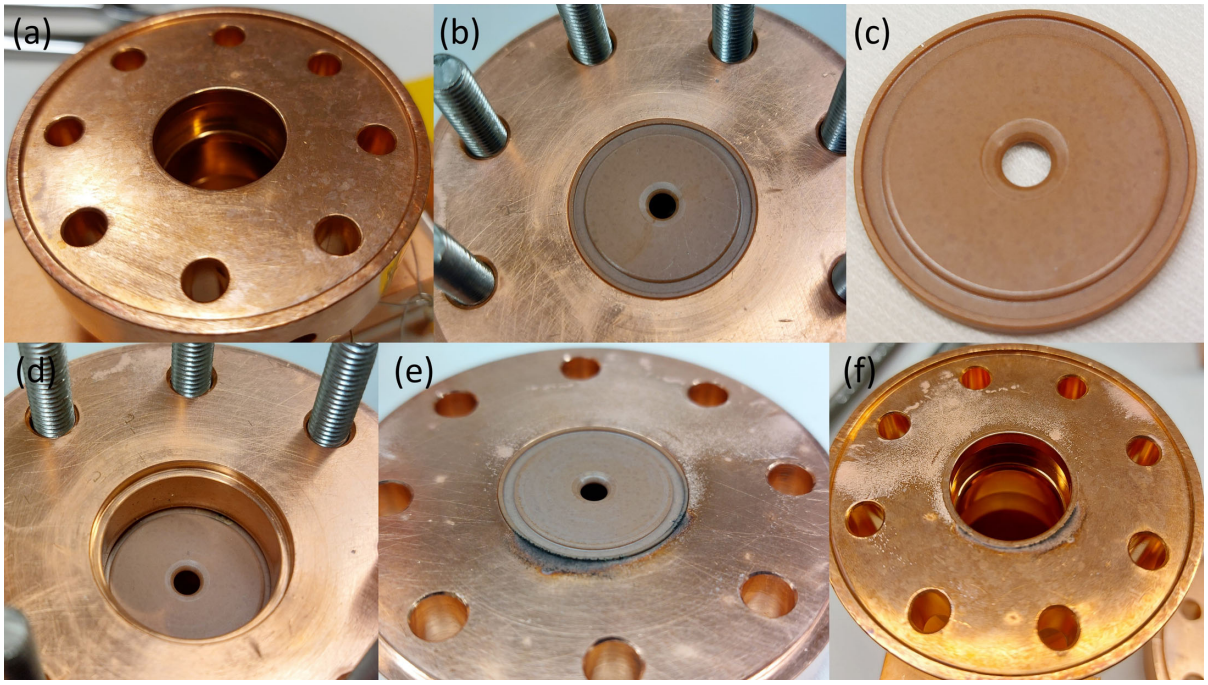

FIG. 26. Posthigh power test inspection photos taken during disassembly of the clamped DDA prototype: upstream matching cell (a); upstream ceramic disk exterior face (b); upstream ceramic interior face (c); downstream ceramic interior face (d); downstream ceramic exterior face (e); and downstream matching cell (f).

IV. CONCLUSION

Two single cell *X*-band dielectric disk accelerating structure prototypes have been tested at high power at the Argonne Wakefield Accelerator. The first prototype, a brazed structure, was limited to 46.6 MV/m accelerating gradient from 79.9 MW input power due to the breakdown at the braze joint. The second prototype possessed an improved design of the triple junction and was assembled by clamping rather than brazing. This DDA structure achieved 102 MV/m accelerating gradient from 321-MW input power. The limit for this structure was the available rf power, not breakdown. A high power test of a multicell DDA structure is planned at the AWA. The good performance of the clamped single cell prototype indicates this technology is suitable for the short rf pulse two-beam acceleration scheme envisioned for the Argonne Flexible Linear Collider.

ACKNOWLEDGMENTS

The work by Euclid Beamlabs LLC was funded through the U.S. Department of Energy (DOE) under Small Business Innovation Research Contract No. DE-SC0019864. The work by the AWA was funded through the U.S. DOE Office of Science under Contract No. DE-AC02-06CH11357. Use of the Center for Nanoscale Materials, an Office of Science user facility, was supported by the U.S. Department of Energy, Office of Science, Office of Basic Energy Sciences, under Contract No. DE-AC02-06CH11357, and under SBIR Phase I Release I 2019, Contract No. DE-SC0019559.

[1] E. R. Colby and L. K. Len, Roadmap to the future, Rev. Accel. Sci. Techol. **09**, 1 (2016).

[2] E. Esarey, C. Schroeder, and W. Leemans, Physics of laser-driven plasma-based electron accelerators, Rev. Mod. Phys. **81**, 1229 (2009).

[3] W. Leemans, A. Gonsalves, H.-S. Mao, K. Nakamura, C. Benedetti, C. Schroeder, C. Tóth, J. Daniels, D. Mittelberger, S. Bulanov *et al.*, Multi-GeV Electron Beams from Capillary-Discharge-Guided Subpetawatt Laser Pulses in the Self-Trapping Regime, Phys. Rev. Lett. **113**, 245002 (2014).

[4] E. Peralta, K. Soong, R. England, E. Colby, Z. Wu, B. Montazeri, C. McGuinness, J. McNeur, K. Leedle, D. Walz *et al.*, Demonstration of electron acceleration in a laser-driven dielectric microstructure, Nature (London) **503**, 91 (2013).

[5] R. J. England, R. J. Noble, K. Bane, D. H. Dowell, C.-K. Ng, J. E. Spencer, S. Tantawi, Z. Wu, R. L. Byer, E. Peralta *et al.*, Dielectric laser accelerators, Rev. Mod. Phys. **86**, 1337 (2014).

[6] M. Hogan, C. Barnes, C. Clayton, F. Decker, S. Deng, P. Emma, C. Huang, R. Iverson, D. Johnson, C. Joshi *et al.*, Multi-GeV Energy Gain in a Plasma-Wakefield Accelerator, Phys. Rev. Lett. **95**, 054802 (2005).

[7] M. Litos, E. Adli, W. An, C. Clarke, C. Clayton, S. Corde, J. Delahaye, R. England, A. Fisher, J. Frederico *et al.*, High-efficiency acceleration of an electron beam in a plasma wakefield accelerator, Nature (London) **515**, 92 (2014).

[8] B. O'Shea, G. Andonian, S. Barber, K. Fitzmorris, S. Hakimi, J. Harrison, P. Hoang, M. Hogan, B. Naranjo, O. Williams *et al.*, Observation of acceleration and deceleration in gigaelectron-volt-per-metre gradient dielectric wakefield accelerators, Nat. Commun. **7**, 12763 (2016).

[9] C. Jing, S. Antipov, M. Conde, W. Gai, G. Ha, W. Liu, N. Neveu, J. Power, J. Qiu, J. Shi *et al.*, Electron acceleration through two successive electron beam driven wakefield acceleration stages, Nucl. Instrum. Methods Phys. Res., Sect. A **898**, 72 (2018).

[10] M. Aicheler, P. Burrows, M. Draper, T. Garvey, P. Lebrun, K. Peach, N. Phinney, H. Schmickler, D. Schulte, and N. Toge, A multi-TeV linear collider based on CLIC technology: CLIC conceptual design report, CERN, Geneva, CERN Yellow Reports: Monographs, Report No. CERN-2012-007, 2012.

[11] B. Cros and P. Muggli, Towards a proposal for an advanced linear collider, in *Report on the Advanced and Novel Accelerators for High Energy Physics Roadmap Workshop, CERN, Geneva* (CERN, Geneva, Switzerland, 2017).

[12] C. Jing, Dielectric wakefield accelerators, Rev. Accel. Sci. Techol. **09**, 127 (2016).

[13] M. Conde, G. Ha, E. Wisniewski, W. Liu, N. Neveu, C. Whiteford, J. Qiu, J. Shao, S. Antipov, L. Zheng *et al.*, Research program and recent results at the Argonne Wakefield Accelerator Facility (AWA), in *Proceedings of the 8th International Particle Accelerator Conference, Copenhagen, Denmark* (JACoW, Geneva, Switzerland, 2017), pp. 2885–2887.

[14] A. Grudiev, S. Calatroni, and W. Wuensch, New local field quantity describing the high gradient limit of accelerating structures, Phys. Rev. ST Accel. Beams **12**, 102001 (2009).

[15] J. Shao, X. Lin, M. Peng, H. Chen, S. Doran, G. Ha, C. Jing, W. Liu, J. Power, J. Shi, C. Whiteford, E. Wisniewski, and H. Zha, Demonstration of gradient above 300 MV/m in short pulse regime using an X-band single-cell structure, in *Proceedings of 13th International Particle Accelerator Conference, IPAC'22, Bangkok, Thailand* (JACoW, Geneva, Switzerland, 2022), pp. 3134–3137.

[16] E. I. Simakov, V. A. Dolgashev, and S. G. Tantawi, Advances in high gradient normal conducting accelerator structures, Nucl. Instrum. Methods Phys. Res., Sect. A **907**, 221 (2018).

[17] W. Gai, J. Power, and C. Jing, Short-pulse dielectric two-beam acceleration, J. Plasma Phys. **78**, 339 (2012).

[18] G. Bruck and E. Wicher, Slow transverse magnetic waves in cylindrical guides, J. Appl. Phys. **18**, 766 (1947).

[19] R. Harvie, A proposed new form of dielectric-loaded waveguide for linear electron accelerators, Nature (London) **162**, 890 (1948).

[20] R. Shersby-Harvie, L. Mullett, W. Walkinshaw, J. Bell, and B. Loach, A theoretical and experimental investigation of anisotropic-dielectric-loaded linear electron accelerators, Proc. IEE B **104**, 273 (1957).

[21] J. Shao, M. Conde, C. Jing, D. Doran, and J. Power, Study of a dielectric disk structure for short pulse two-beam acceleration, in *Proceedings of the 9th International Particle Accelerator Conference, Vancouver, BC, Canada* (JACoW, Geneva, Switzerland, 2018), pp. 1539–1541.

[22] C. Jing, J. Shao, J. Power, M. Conde, and S. Doran, Dielectric disk accelerator for high gradient short pulse two-beam wakefield acceleration, in *2018 IEEE Advanced Accelerator Concepts Workshop (AAC)* (IEEE, New York, 2018), pp. 1–5.

[23] Y. Wei, H. Bursali, A. Grudiev, B. Freemire, C. Jing, R. Wegner, J. S. Bedolla, and C. Welsch, Design, fabrication, and low-power rf measurement of an *x*-band dielectric-loaded accelerating structure, Phys. Rev. Accel. Beams **25**, 041301 (2022).

[24] J. Krupka, K. Derzakwoski, B. Riddle, and J. Baker-Jarvis, A dielectric resonator for measurements of complex permittivity of low loss dielectric materials as a function of temperature, Meas. Sci. Technol. **9**, 1751 (1998).

[25] CST Studio, CST, Bad Nauheimer Str. 19, 64289 Darmstadt, Germany.

[26] COMSOL Multiphysics®, COMSOL AB, Stockholm, Sweden.

[27] J. Shi, H. Chen, X. Wu, C. Jing, Y. Yang, W. Gai, Q. Gao, and H. Zha, Development of an x-band metallic power extractor for the Argonne Wakefield Accelerator, in *Proceedings of the 4th International Particle Accelerator Conference, IPAC-2013, Shanghai, China* (JACoW, Geneva, Switzerland, 2013), pp. 2771–2773.

[28] M. Peng, J. Shao, C. Jing, E. Wisniewski, G. Ha, J. Seok, M. Conde, W. Liu, J. Power, S. Doran, C. Whiteford, J. Shi, H. Zha, and H. Chen, Generation of high power short rf pulses using an x-band metallic power extractor driven by high charge multi-bunch train, in *Proceedings of the 10th International Particle Accelerator Conference, IPAC-2019, Melbourne, Australia* (JACoW, Geneva, Switzerland, 2019).

[29] J. Shao, C. Jing, E. Wisniewski, G. Ha, M. Conde, W. Liu, J. Power, and L. Zheng, Development and high-power testing of an *x*-band dielectric-loaded power extractor, Phys. Rev. Accel. Beams **23**, 011301 (2020).

[30] S. Mori, M. Yoshida, and D. Satoh, The design optimization of the dielectric assist accelerating structure for better heat and gas transfer, in *Proceedings of the 10th International Particle Accelerator Conference, IPAC-2019, Melbourne, Australia* (JACoW, Geneva, Switzerland, 2019), pp. 1179–1181.

[31] S. Mori, M. Yoshida, and D. Satoh, Wakefield damping in the dielectric assist accelerating structure, in *Proceedings of 16th Annual Meeting of Particle Accelerator Society of Japan PASJ'19, Kyoto, Japan* (2019), pp. 1034–1037.

[32] B. J. Munroe, A. M. Cook, M. A. Shapiro, R. J. Temkin, V. A. Dolgashev, L. L. Laurent, J. R. Lewandowski, A. D. Yeremian, S. G. Tantawi, and R. A. Marsh, High power breakdown testing of a photonic band-gap accelerator structure with elliptical rods, Phys. Rev. ST Accel. Beams **16**, 012005 (2013).

[33] J. Zhang, B. J. Munroe, H. Xu, M. A. Shapiro, and R. J. Temkin, High power experimental studies of hybrid

photonic band gap accelerator structures, Phys. Rev. Accel. Beams **19**, 081304 (2016).

[34] https://www.bergoz.com/en/ict-bcm-ihr.

[35] J. G. Power, W. Gai, S. H. Gold, A. K. Kinkead, R. Konecny, C. Jing, W. Liu, and Z. Yusof, Observation of Multipactor in an Alumina-Based Dielectric-Loaded Accelerating Structure, Phys. Rev. Lett. **92**, 164801 (2004).

[36] D. Caballero, W. Wuensch, K. Szypula, N. Lasheras, B. Gimeno, and A. Golfe, Combined field emission and multipactor simulation in high gradient rf accelerating structures, in *Proceedings of the 10th International Particle Accelerator Conference, IPAC-2019, Melbourne, Australia* (JACoW, Geneva, Switzerland, 2019), pp. 2940–2943.

[37] E. Tulu, U. van Rienen, and A. Arnold, 3D multipacting study for the Rossendorf SRF gun, in *Proceedings of SRF'13* (JACoW, Geneva, Switzerland, 2013), pp. 991–994.

[38] V. Ivanov, A. Sakharov, and M. Konyzhev, Theoretical and experimental study of multipactor discharge on a dielectric, J. Phys. Conf. Ser. **1094**, 012026 (2018).

[39] M. Gusarova, V. Kaminsky, S. Kutsaev, M. Lalayan, N. Sobenin, L. Kravchuk, and S. Tarasov, Multipacting simulation in rf structures, in *Proceedings of LINAC'08, Victoria, BC, Canada* (TRIUMF, Vancouver, BC, Canada, 2008), pp. 266–268.

[40] S. V. Langellotti, N. M. Jordan, Y. Y. Lau, and R. M. Gilgenbach, CST particle studio simulations of coaxial multipactor and comparison with experiments, IEEE Trans. Plasma Sci. **48**, 1942 (2020).

[41] A. Sazontov and V. Nevchaev, Effects of rf magnetic field and wave reflection on multipactor discharge on a dielectric, Phys. Plasmas **17**, 033509 (2010).

[42] J. Power, High gradient research activities at AWA, in *Proceedings of International Workshop on Breakdown Science and High Gradient Technology* (2021), https://indico.fnal.gov/event/22025/contributions/210368/attachments/142268/179578/JohnPower-AWA-HG21.pdf.

[43] C. Jing, W. Gai, J. G. Power, R. Konecny, S. H. Gold, W. Liu, and A. K. Kinkead, High-power rf tests on x-band dielectric-loaded accelerating structures, IEEE Trans. Plasma Sci. **33**, 1155 (2005).

[44] C. Jing, W. Gai, J. G. Power, R. Konecny, W. Liu, S. H. Gold, A. K. Kinkead, S. G. Tantawi, V. Dolgashev, and A. Kanareykin, Progress toward externally powered x-band dielectric-loaded accelerating structures, IEEE Trans. Plasma Sci. **38**, 1354 (2010).

[45] C. Jing, S. Antipov, P. Schoessow, A. Kanareykin, J. Power, M. Conde, and W. Gai, Argonne flexible linear collider, in *Proceedings of the 4th International Particle Accelerator Conference, IPAC-2013, Shanghai, China* (JACoW, Geneva, Switzerland, 2013) pp. 1322–1324.